An INSPECT Measurement System for Moving Objects

Fuqin Deng, Chang Liu, Wuifung Sze, Jiangwen Deng, Kenneth S. M. Fung, and Edmund Y. Lam, *Senior Member, IEEE*

***Abstract*— Noncontact optical imaging is frequently used in the inspection and metrology of stationary objects, including in particular the reconstruction of the 3-D surface profile. A technique, known as phase-measuring profilometry, involves projecting a sinusoidal pattern and then inferring the height of various points on the object by measuring the resulting phase changes at the respective locations. However, this method cannot be directly applied to systems involving moving objects, as the translation and the perspective geometry effect manifest as errors in the height calculations. In this paper, we report on an imaging and numerical surface profilometry with error compensation technology (INSPECT) measurement system that is tailored for moving objects. We model the imaging system that considers the nonlinear perspective geometry effect, and simplify to a first-order equation using Taylor series expansion. With this, we generalize the conventional phase shift algorithm, and develop the optimization procedures that can compute the height information effectively. We apply this technology to the INSPECT measurement system in semiconductor manufacturing and show significant improvement in accuracy and robustness.**

***Index Terms*— 3-D image acquisition, fringe pattern analysis, fringe pattern profilometry, image reconstruction, industrial inspection, surface measurement.**

I. Introduction

VISUAL inspection and metrology are the key steps in many manufacturing operations, and developing machine vision systems for such tasks demands continuous research and development to cope with the constantly tightening specifications [1]. A specific case is the semiconductor industry, where the complex manufacturing process is divided into the front and the back end [2], [3]. The former includes procedures such as optical lithography, ion implantation, and etching, and requires monitoring of wafer flatness and thickness uniformity, mask defect detection, and hotspot detection in the circuit pattern [4], to name a few inspection and metrology tasks. As for back end, the major steps are assembly and packaging, and they involve steps such as die bonding, wire bonding, and integrated circuit (IC) encapsulation. Certain advanced packaging types such as ball grid array, which is a form of surface-mount technology (SMT), often require 3-D inspection and metrology, specifically in producing the surface profile of the connectors for bonding or the epoxy adhesive. This is the focus of this paper.

There are at least three conflicting requirements for the design of the imaging instrument and the associated algorithms for semiconductor assembly and packaging inspection.

1) The IC dies contain small feature sizes, requiring a high precision in metrology.
2) There is often a need for inspecting a large field of view (FOV).
3) The sheer volume of inspection demands a high throughput on the production line.

In this paper, we want to include a fourth requirement, which is that the item being inspected is moving on a conveyor belt. This is conducive to enhancing the throughput of the whole system, at the expense of requiring extra computation in adjusting for the object position when multiple images are taken. Moreover, some error sources such as the perspective geometry effect may cause inaccurate surface profilometry of moving objects. Thus, our objective is to develop an imaging and numerical surface profilometry with error compensation technology (INSPECT) measurement system, for high-resolution, high-precision, and dense surface profilometry of moving objects, and then apply it in semiconductor back end manufacturing and assembly applications.

We should note that some 3-D imaging techniques and systems have already been commercialized for metrology applications over the years [5]; nevertheless, many of them cannot meet the ever-increasing requirements of precision and speed from the semiconductor industry. These systems are based on a variety of optical noncontact approaches, including, for instance, shape from shading, stereo, depth from focus, confocal imaging, and time-of-flight, each with some shortcomings. The first one, shape from shading, is intrinsically ill-posed, and it has been argued that most of the assumptions are inappropriate for surface reconstruction in a real environment [6]. Area-based stereo, using multiple cameras, can obtain a dense surface map, but this approach fails at featureless regions [7]. Depth from focus provides

Manuscript received October 28, 2013; revised March 29, 2014; accepted May 8, 2014. Date of publication July 10, 2014; date of current version December 5, 2014. This work was supported in part by ASM Pacific Technology Ltd., Hong Kong, in part by the Research Grants Council of the Hong Kong Special Administrative Region under Project HKU 7138/11E and Project 7131/12E, and in part by the University Research Committee, University of Hong Kong, Hong Kong, under Project 104003115. The Associate Editor coordinating the review process was Zheng Liu.

F. Deng is with the Imaging Systems Laboratory, Department of Electrical and Electronic Engineering, University of Hong Kong, Hong Kong, and also with ASM Pacific Technology Ltd., Hong Kong.

C. Liu, W. Sze, J. Deng, and K. S. M. Fung are with ASM Pacific Technology Ltd., Hong Kong.

E. Y. Lam is with the Imaging Systems Laboratory, Department of Electrical and Electronic Engineering, University of Hong Kong, Hong Kong (e-mail: elam@eee.hku.hk).

Color versions of one or more of the figures in this paper are available online at http://ieeexplore.ieee.org.

Digital Object Identifier 10.1109/TIM.2014.2329387

a powerful means of recovering the high-resolution shapes of rough surfaces through an objective lens with a large numerical aperture. However, it cannot determine the depth of a homogeneous surface without visible contrast variation [8]. Confocal imaging is able to reconstruct an object profile with a high precision, but it is not suitable for high-speed measurement due to its sequential acquisition. While laser triangulation projects lines or a dot matrix pattern to reduce the scanning process [9], speckle is inevitable in the captured data, and results in a fundamental uncertainty in the surface measurement. Finally, the time-of-flight camera makes it possible to capture the depth image in real-time [10], but there exists error caused by multiple reflections of the active light inside and outside the camera.

Aside from these approaches, phase-measuring profilometry (PMP) is another surface measurement technique, which involves projecting a known fringe pattern on the object and detecting the phase changes from the captured images, with which one can infer the object height at different locations. In our view, this method is most amenable to our application requirements [11]. There are two principal ways to create the fringe pattern. First, it can be generated by the interference of coherent light waves. This can achieve nanometer resolution for surface topography, but the measuring range is limited by the source wavelength, and a computationally intensive phase unwrapping step is needed when the height range is larger than the wavelength [12]. Moreover, the fringe pattern generated from interference is very sensitive to vibration, which limits its applications to vibration-free environment. Second, the fringe pattern can be customized using gratings or digital light processing projectors [13]. In its design, we can actively control the frequency of the fringe pattern to avoid the need for phase unwrapping. In addition, this method allows for measuring the shape of an object even in the absence of high-contrast feature points. Our technique follows the second approach.

In what follows, we first give a brief overview of the PMP technique, explaining in particular the algorithm to reconstruct the height information. We will then discuss the additional requirement of measuring moving objects, and present our technique that can solve this problem.

II. Phase-Measuring Profilometry

A. Imaging Model and the Surface Reconstruction Algorithm

Since for each row of the projected sinusoidal patterns, the phase varies in a similar manner, we label this direction as the x-direction, and consider the cross-sectional reconstruction of the object surface on the xz plane. The same procedure can be applied for different values of y, its orthogonal direction [14]. Furthermore, this cross-sectional reconstruction procedure also works even if there is a rotation between the projected fringe pattern and the chosen coordinate system. To simplify the discussions, in the following, we designate the 3-D coordinate of a point with its x- and z-coordinate only.

Now, consider a specific point of the object at coordinate x_0, with height $h(x_0)$. The phase of the sinusoid projected on this point is a function of these two quantities, denoted as

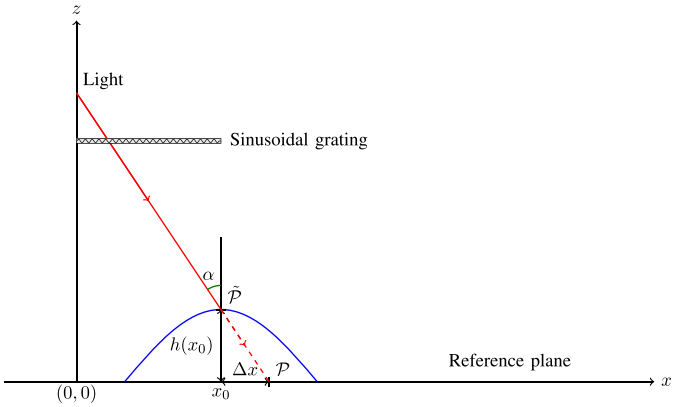

Fig. 1. Phase offset due to height variation in surface profilometry.

$\phi(x_0, h(x_0))$. The intensity of the captured image at this location, $I(x_0)$, is then a function of this phase, as well as two other quantities, the background intensity $B(x_0)$ and the fringe contrast $C(x_0)$, given by

$$I(x_0) = B(x_0) + C(x_0)\cos\phi(x_0, h(x_0)) + N(x_0) \quad (1)$$

where $N(x_0)$ is the additive noise at this location.

The task is then to model the relationship between the phase and the height at the reconstruction location. In a telecentric projection and imaging system, when the sinusoidal grating is orthographically projected onto the whole measuring space with an incident angle α, the phase $\phi(x_0, h(x_0))$ changes linearly according to the displacement of the reconstructed point along the x- and z-direction, respectively. Denoting the spatial frequency along the x-direction as f_x, we can model the phase on the reference plane by

$$\phi(x_0, 0) = 2\pi f_x x_0. \quad (2)$$

As shown in Fig. 1, the incoming light, modulated by the sinusoidal grating, illuminates the point $\tilde{\mathcal{P}}$ on the reconstructed object. If the object were absent, this light would illuminate the point $\mathcal{P}$ instead on the reference plane. Based on the triangular relationship, the offset of the illuminated point would be

$$\Delta x = h(x_0)\tan\alpha \quad (3)$$

and the corresponding phase offset would be $2\pi f_x \Delta x$. Let the $f_z = f_x \tan\alpha$, then the phase at the point $(x_0, h(x_0))$ is then given by

$$\phi(x_0, h(x_0)) = 2\pi f_x x_0 + 2\pi f_x \Delta x = 2\pi f_x x_0 + 2\pi f_z h(x_0). \quad (4)$$

With this linear relationship between the height and the phase, at a given location x_0, one can reconstruct the height from its phase efficiently [15].

The goal of a phase-shift algorithm (PSA) is to deduce the phase, and subsequently the height, of all points from the captured image given by (1). Since we are dealing with all the points, we can drop the subscript in x_0. On the other hand, we want to eliminate the contributions of the background intensity and fringe contrast in our observed image. In theory, this is possible by capturing two additional images with different phase patterns; in practice, acquiring altogether four images

seems to be the minimal requirement. Accordingly, we rewrite (1) as

$$I_k(x) = B(x) + C(x)\cos\phi_k(x, h(x)) + N_k(x) \tag{5}$$

where $k = 1, \ldots, n$, and n is the total number of images acquired for postprocessing. Note that the background intensity and fringe contrast are independent of k.

The next major task is to model these different phase patterns. Let us denote the relative phase shift of the kth image be θ_k, with $\theta_1 = 0$ as the reference. Then

$$\phi_k(x, h(x)) = \phi(x, h(x)) + \theta_k. \tag{6}$$

We need to choose a set of θ_k that are both practical to realize and mathematically convenient to process. Regarding the former question, physically, there are two ways to create these phase shifts. First, we can keep the object stationary, and move the sinusoidal grating through a piezoelectric transducer. However, the nonlinearity of the transducer will introduce phase shift errors during the reconstruction process. Another issue is that we can only reconstruct the surface within a small FOV. Second, we can keep the grating fixed, and move the object by an amount equal to s_k along the x-direction. In this case, $\theta_k = 2\pi f_x s_k$. Regarding the latter consideration, a particularly common choice for s_k is to shift uniformly within one period of the sinusoid, such that $\theta_k = (k-1)\pi/2$. It is sufficient to note that, with four images, a possible way to recover the wrapped phase is

$$\phi(x, h(x)) = \arctan\left\{\frac{I_4(x) - I_2(x)}{I_1(x) - I_3(x)}\right\}. \tag{7}$$

Unwrapping this phase and putting it into (4), we can reconstruct the height of a surface point-by-point for inspection and metrology tasks.

B. Error Sources

We note immediately that the above methodology is derived under an ideal environment; in practice, there are various sources of error that render this approach less accurate or effective. There have been studies aiming at identifying the origin and extent of these errors, while also developing techniques to mitigate their effects, either with computational methods or changes in the physical setup [16].

Intensity fluctuations due to mechanical vibrations and other sources are commonly observed in practical PMP setups, and mathematical approaches using a Taylor series expansion [17] or Fourier analysis have shown good results in suppressing these effects. Along a similar vein, the nonlinear gamma effect has also been incorporated into a mathematical imaging model [18], while a method to eliminate the high-order harmonic components within the fringe patterns has been developed [19]. In addition, there are applications where the captured images have low fringe contrast or uneven illumination; it is shown that one effective way to improve the accuracy of the reconstruction results under this situation is to incorporate the local smoothness of the object surface into a regularized PSA or an illumination-invariant PSA [15]. Recently, it was also shown that a micro phase shift technique can be used to handle a variety of global illumination issues, such as interreflections, subsurface scattering, and defocus [20].

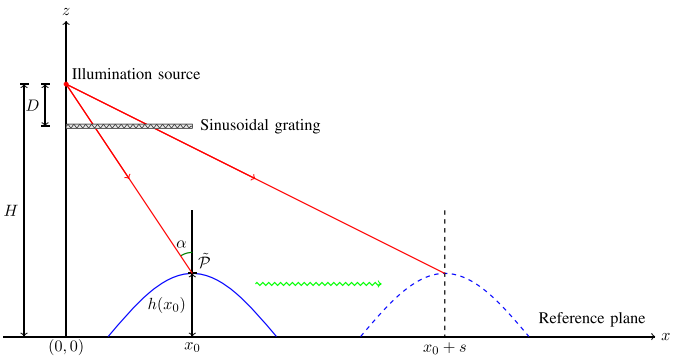

Fig. 2. Perspective model for surface profilometry of a moving object.

Another issue with the ideal setup that may not be practical is the requirement of uniform shifts within one period of the sinusoidal pattern. It is, however, possible to relax this, such as using a random PSA [21] derived under the assumption of randomly shifted sinusoidal patterns. Combining PSA with amplitude modulation also makes it possible to handle the phase unwrapping problem when the height change is beyond what one period of the sinusoidal pattern would cause [22].

C. Perspective Geometry Effect

As mentioned earlier, the primary objective of this paper is to develop an INSPECT measurement system for PMP of moving objects. In most of the projection systems, a major error source is the perspective geometry effect, which affects the deformation measurements of curved surfaces considerably [23]. This is because ordinarily, the phase shifts are assumed to be uniform at different heights [13]. To reduce the perspective projection effect, we can use a telecentric system by design, but the bulky size of the telecentric system is not suitable for applications in the semiconductor inspection and assembly line. The fabricated optical system in practice may not be perfectly telecentric due to manufacturing and assembly tolerances. However, for objects moving on a conveyor belt, the error associated with the assumption of orthographic projection becomes significant, especially for high-precision metrology applications.

To better illustrate the phase distribution under a perspective projection system, we first consider a special configuration with the grating plane being parallel to the reference plane. Later, by a simple matrix transformation of the homogenous coordinates, the phase distribution can be derived under general configurations, including the grating plane being slant to the reference plane. Fig. 2 shows the perspective projection model, for a point at coordinate x_0. A sinusoidal grating with a spatial frequency f_g is used to project the fringe pattern onto the reconstructed surface, while the illumination source is at a distance H from the reference plane and a distance D above the sinusoidal grating. Now, if there is no object at this location, the incoming light would illuminate the reference plane. By similar triangles, the demagnification of the grating with

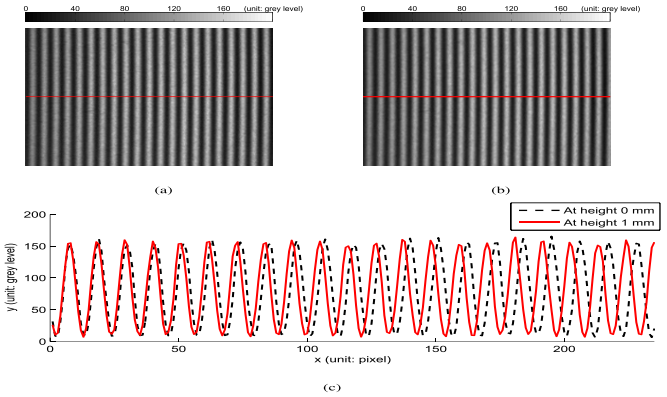

Fig. 3. Projected pattern at different heights. (a) and (b) Images of a homogeneous surface at $z = 0$ and $z = 1$ mm, respectively. (c) Cross-sectional intensity profiles from the middle rows of (a) and (b) (marked in red).

respect to the projected pattern is therefore D/H. Then, the spatial frequency of the projected fringe pattern on the reference plane is

$$f_x = \frac{D}{H} f_g \tag{8}$$

and the phase at the location x_0 is given by

$$\phi(x_0, 0) = 2\pi \left(\frac{D}{H} f_g \right) x_0. \tag{9}$$

On the other hand, if there is an object of height $h(x_0)$ at this location, the incoming light would image the point $\tilde{\mathcal{P}}$ instead. Following a similar derivation, the phase at this point is given by:

$$\phi(x_0, h(x_0)) = 2\pi \left(\frac{D}{H - h(x_0)} f_g \right) x_0. \tag{10}$$

Thus, we can observe that the spatial frequency of the sinusoidal pattern effectively encodes the object height. Note that the derivation in Section II-A ignores this dependence on height and assumes the same frequencies f_x and f_z along x- and z-direction throughout. However, in a perspective projection system, these spatial frequencies vary according to the position of the illuminated point.

When the object is translated by an amount s in the positive x-direction, the corresponding phase shifts are given by

$$\phi(x_0 + s, 0) - \phi(x_0, 0) = 2\pi \left(\frac{D}{H} f_g \right) s \tag{11}$$

and

$$\phi(x_0 + s, h(x_0)) - \phi(x_0, h(x_0)) = 2\pi \left(\frac{D}{H - h(x_0)} f_g \right) s \tag{12}$$

respectively. This means that the period of the resulting sinusoid varies with the height. Fig. 3 shows this with a physical experiment. A homogeneous plane is first assumed to be at the focal plane of the projection system, and the captured image is shown in Fig. 3(a). Using this as the reference plane with $h = 0$ mm, we offset it by 1 mm in the z-direction and capture another image of the fringe patterns, as shown in Fig. 3(b). We then compare the normalized cross-sectional intensity profiles from the middle row of these two images, as shown in Fig. 3(c). While they align with each other on the left, due to different spatial frequencies at different heights, the two sinusoids increasingly depart from each other at larger distances. Thus, for example, when the points on the left move by $s = 200$ pixels to the right, the phase shift difference caused by the nonuniformity of the phase distribution is around one-third of a period using (12). Therefore, we can conclude that when reconstructing the surface of a moving object, we need to take this phase shift variation into account in designing the appropriate PSA.

III. Polynomial PMP Model

A. Imaging Model Formulation

In reality, the grating may not be parallel to the reference plane, making it difficult to measure the distances D and H for calibrating the perspective model of the projector based on the discussions above. While a method that uses an extra programmable LCD panel for the calibration exists [24], often a purely computational approach, which does not involve changing the physical system, is more desirable [25]. A further complication is establishing the relationship between the image intensity and the phase distribution when both the projection system and the imaging system are perspective. To simplify the description of phase distribution, we use a polynomial to model the above phase distribution first. Then, the phase distribution in the general configurations can be derived based on a simple matrix transformation of the homogenous coordinates. From (10) and (12), it is possible to formulate the perspective geometry-dependent parameter at x_0 as a function of $h(x_0)/H$. This is because using the Taylor series expansion, we have

$$\begin{aligned} \frac{D}{H - h(x_0)} &= \frac{D}{H} \left(1 - \frac{h(x_0)}{H} \right)^{-1} \\ &= \frac{D}{H} \left[1 + \frac{h(x_0)}{H} + \mathcal{O}\left(\frac{h^2(x_0)}{H^2} \right) \right] \end{aligned} \tag{13}$$

provided that $h(x_0) \ll H$. This assumption is valid for our purpose of inspecting semiconductor component surfaces, where variations in height is usually minute compared with the positioning of the light source, and may also be applicable for other similar inspection and metrology tasks. In a similar manner, the above Taylor series can be decomposed further and more terms of the Taylor series are then obtained to model the perspective projection effect when needed. In our application, if we ignore the higher order terms in the above expression, the phase distribution becomes

$$\begin{aligned} \phi(x_0, h(x_0)) &= 2\pi \left(\frac{D}{H - h(x_0)} f_g \right) x_0 \\ &\approx 2\pi \left(\frac{D}{H} f_g \right) x_0 + 2\pi \left(\frac{Dh(x_0)}{H^2} f_g \right) x_0. \end{aligned} \tag{14}$$

This concise expression is possible because the chosen reference plane and the grating plane are parallel. However, in reality, the grating plane may be slant to the reference plane or the object may be set on a general plane instead of this reference plane. Therefore, it is advantageous to write

this equation in a quadratic form using matrices and vectors. Allowing

$$\mathbf{u_0} = \begin{bmatrix} x_0 \\ h(x_0) \\ 1 \end{bmatrix} \quad \text{and} \quad \mathsf{W} = \begin{bmatrix} 0 & \pi \frac{D}{H^2} f_g & \pi \frac{D}{H} f_g \\ \pi \frac{D}{H^2} f_g & 0 & 0 \\ \pi \frac{D}{H} f_g & 0 & 0 \end{bmatrix} \quad (15)$$

where the vector $\mathbf{u_0}$ is known as the homogeneous coordinate of the point $\tilde{\mathcal{P}}$ in Fig. 2, we can write the phase at x_0 compactly as

$$\phi(x_0, h(x_0)) = \mathbf{u_0}^T \mathsf{W} \mathbf{u_0}. \quad (16)$$

In other configurations, such as the grating plant being slant to the reference plane and different coordinate systems being adopted, the phase distribution will change accordingly. Nevertheless, a matrix multiplication can be used to model the relative transformation from a general coordinate system to the current coordinate system [26]. Denoting this transformation matrix as R and assuming the homogeneous coordinate of the reconstructed point $\tilde{\mathcal{P}}$ to be $\tilde{\mathbf{u}}_\mathbf{0} = [\tilde{x}_0 \quad \tilde{h}(\tilde{x}_0) \quad 1]^T$ in the general coordinate system, we have $\mathbf{u_0} = \mathsf{R}\tilde{\mathbf{u}}_\mathbf{0}$. Accordingly, the phase can also be expressed by a quadratic form of the corresponding homogeneous coordinate

$$\phi(\tilde{x}_0, \tilde{h}(\tilde{x}_0)) = (\mathsf{R}\tilde{\mathbf{u}}_\mathbf{0})^T \mathsf{W} (\mathsf{R}\tilde{\mathbf{u}}_\mathbf{0}) = \tilde{\mathbf{u}}_\mathbf{0}^T (\mathsf{R}^T \mathsf{W} \mathsf{R}) \tilde{\mathbf{u}}_\mathbf{0}. \quad (17)$$

We can let $\widetilde{\mathsf{W}} = \mathsf{R}^T \mathsf{W} \mathsf{R}$. Since W is a symmetric matrix, $\widetilde{\mathsf{W}}$ is, too.

At this point, we would like to make two notational simplifications for the rest of this paper. First, we would use $\tilde{w}_{ij}$ to refer to the entry of $\widetilde{\mathsf{W}}$ at the ith row and jth column. Since this is a 3×3 matrix, $1 \leq i, j \leq 3$. We also let $\omega_{xx} = \tilde{w}_{11}$, $\omega_{xz} = \tilde{w}_{12} + \tilde{w}_{21}$, $\omega_{zz} = \tilde{w}_{22}$, $\omega_x = \tilde{w}_{13} + \tilde{w}_{31}$, $\omega_z = \tilde{w}_{23} + \tilde{w}_{32}$, and $\omega_0 = \tilde{w}_{33}$. Second, since we are dealing with all the points, we can drop the superscript and subscript in $\tilde{x}_0$. With these simplifications, the above expression of the phase can be represented as

$$\phi(x, h(x)) = \omega_{xx} x^2 + \omega_{xz} x h(x) + \omega_{zz} h^2(x) + \omega_x x + \omega_z h(x) + \omega_0. \quad (18)$$

We call such polynomial formulation of the phase distribution as polynomial PMP (P-PMP) model.

B. Advantages

There are several advantages of using the P-PMP model to describe the phase distribution within the measuring space.

First, this model unifies both the orthographic model and the perspective model in the same framework by a polynomial formulation. The orthographic model in (4), can be considered a special case of the P-PMP model, with $\omega_x = 2\pi f_x$, $\omega_z = 2\pi f_z$, and zeros for the other terms. In this scenario, for surface profilometry of a moving object, we can efficiently decompose the phase into two parts: the phase shift due to the movement of the object and the phase offset caused by the height variation on the reconstructed surface. This decomposition helps us to formulate and solve the reconstruction problem efficiently based on the matrix and vector form. However, using this orthographic model, we cannot get high-precision surface profile in many perspective projection systems for industrial metrology. Therefore, we incorporate the high-order polynomial terms in our P-PMP model so that we can model the phase distribution effectively under a perspective projection system and develop an error compensation technique later for high-precision surface profilometry of a moving object.

Second, by simplifying the expression for the nonlinear phase distribution with a polynomial form, the calibration for phase distribution in the following section is a simple polynomial fitting process, which minimizes the summed square of the residuals for all the measured points. After calibration, the phase in this polynomial form, can also be decomposed efficiently into two parts in formulating and solving the reconstruction problem as the orthographic model does. Moreover, there are physical meanings for the coefficients in the P-PMP model. For example, ω_x is the spatial angular frequency of the projected fringe pattern along x-direction at the reference point. Even though the intrinsic and extrinsic parameters of the projection system are not known, we can still quantify and then analyze the phase variation at each position by these coefficients in the model. At $(x, h(x))$, let us denote the spatial angular frequency as $F_x(x, h(x))$ and the fringe period as $T_x(x, h(x))$, such that $T_x(x, h(x)) = 2\pi / F_x(x, h(x))$. This position-dependent spatial angular frequency can be readily computed by

$$F_x(x, h(x)) = \frac{\partial \phi(x, h(x))}{\partial x} = \omega_x + 2\omega_{xx} x + \omega_{xz} h(x). \quad (19)$$

Furthermore, within a measuring range of the INSPECT system, we can measure the extent of the perspective geometry effect by considering the fringe periods at all possible $(x, h(x))$ to compute the magnification variation M, where

$$M = \frac{\max T_x(x, h(x)) - \min T_x(x, h(x))}{\min T_x(x, h(x))}. \quad (20)$$

This value is an important factor to judge the performance of the system for dimensional measurement. We will use it in later experiments for comparing the performance at different extents of perspective projection effect. In our specific second-order P-PMP model, the phase distribution is concisely represented by a quadratic form. With simple matrix transformations, we can efficiently obtain the phase distribution under other coordinate systems or configurations.

In conventional methods for surface profilometry, multiple images with different phase shifts are needed to be projected onto a static object, which causes the phase distribution changes accordingly. In contrast, the proposed method only requires projecting a single fringe pattern, and then the P-PMP model for the global description of the phase distribution remains the same after the optical system has been fixed. This simplification facilitates the reconstruction of a moving object in our INSPECT system if the phase distribution has been calibrated beforehand.

IV. Polynomial Phase Shift Algorithm

In developing the In developing the polynomial PSA (P-PSA), we formulate the surface reconstruction of a moving object as an optimization problem using the P-PMP model. To make this nonlinear optimization problem

more tractable, we divide the height estimation into four steps.

1) We calibrate the P-PMP model for the stationary vision system, so that we have the coefficients of the polynomial for describing the phase distribution in the whole measuring space.
2) With this calibrated imaging model, we estimate the phase shifts caused by motion. Since the reconstructed height $h(x)$ is involved in this nonlinear model, to get a good initial value, which helps to converge to the right solution more quickly, we use an approximated polynomial model to estimate the phase shifts, and then solve for an initial estimate of the height.
3) With this estimate, we compensate the phase shift error due to the perspective geometry effect from the projection system.
4) We use the refined phase shifts to estimate the height for each reconstructed point.

This numerical surface profilometry with error compensation technology can be integrated into the INSPECT system for surface profilometry of moving objects.

We now explain these steps in more details. Unlike many conventional PSAs where the formulations vary significantly with the number of images used for reconstruction, the proposed P-PSA can recover the height-related phase in a similar fashion with $n \geq 3$ images at different phase shifts. Since the INSPECT system is stationary and the projected sinusoidal pattern is fixed, the phase distribution $\phi(x, h(x))$ remains the same during surface profilometry. When an object moves from x to $x + s_k$, where $k = 1, \ldots, n$, its phase value becomes $\phi(x + s_k, h(x))$. Similar to the imaging model described in Section I, under additive noise $N_k(x)$, the image intensity for the reconstructed point x can be modeled by

$$I_k(x) = B(x) + C(x) \cos \phi(x + s_k, h(x)) + N_k(x). \quad (21)$$

Now, let $E_k(x, h(x))$ be the residual error of the imaging model

$$E_k(x, h(x)) = I_k(x) - B(x) - C(x) \cos \phi(x + s_k, h(x)). \quad (22)$$

With this, we can formulate the phase reconstruction as an optimization problem in which the optimal height $h(x)$ at location x can be obtained by minimizing

$$E(x, h(x)) = \sum_{k=1}^{n} E_k^2(x, h(x)). \quad (23)$$

Note that $B(x)$, $C(x)$, $h(x)$, and $\phi(x + s_k, h(x))$ are unknown in this formulation. However, only the image intensity $I_k(x)$ and the motion movement s_k are available now, which can be read from the image sensor and position sensor, respectively. Such a little information is generally not enough for solving this nonlinear optimization problem effectively. Thus, we need to calibrate the P-PMP model beforehand, and then use the calibrated coefficients as the prior knowledge to simplify the optimization problem.

During the calibration step, we put a homogeneous plane at the focal plane of the given INSPECT measurement system, assuming it to be the reference plane with height $h_1 = 0$ mm.

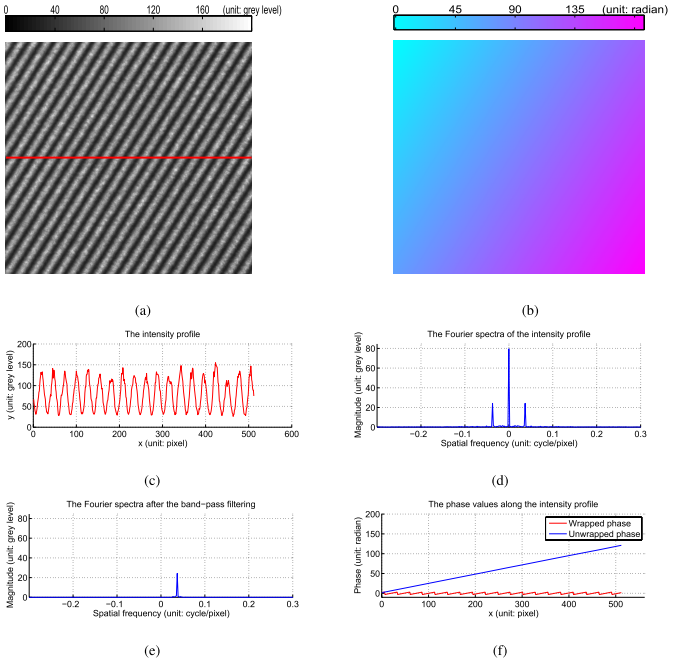

Fig. 4. Phase estimation on a homogeneous plane based on FFT.

Normally, multiple patterns with different phase shifts are projected onto this plane, and the corresponding images are then captured for phase estimation [27]. However, the phase shift error between these patterns may introduce a systematic error during calibration. Since the plane is homogeneous, the background intensity and the fringe contrast can be assumed to be constants, fast Fourier transform (FFT) is a more efficient alternative to obtain the phase with only one image. Fig. 4(a) and (b) shows a real image on a homogenous steel plate and the unwrapped phase on this plane, respectively. Fig. 4(c)–(f) shows the phase estimation process with a cross-sectional intensity profile, marked in red in (a). This cross section and its Fourier spectra by FFT are shown in Fig. 4(c) and (d), respectively. After using a bandpass filter to select either of the spectra modulated by the fringe patterns in Fig. 4(e), we apply the inverse FFT to the selected spectra, and compute the logarithm of the resulting complex quantities. The wrapped phase values are then extracted from their imaginary parts [28]. Since there is no phase jump larger than π, between the neighboring pixels on this homogenous plane, in Fig. 4(f), we add the phase 2π at the discontinuous positions to get the unwrapped phase along this cross section.

Similarly, we offset this homogeneous plane to m different positions along the z-direction, at the height of h_j, where $j = 1, \ldots, m$ and capture an image at each position. Since we are using a second-order polynomial in the P-PMP model, at least three such images ($m \geq 3$) at different heights are needed during this calibration step. With all the phase values $\phi(x, h_j)$ at (x, h_j) on these calibration planes, we can estimate the coefficients of the proposed P-PMP model by fitting the second-order polynomial model in (18).

Next, in Step 2, with a calibrated INSPECT system, our goal is to estimate the phase shifts caused by motion. When

the reconstructed object moves from x to $x + s_k$, the phase shift, denoted as $\theta(x, h(x), s_k)$, can be calculated by

$$\begin{aligned}\theta(x, h(x), s_k) &= \phi(x + s_k, h(x)) - \phi(x, h(x)) \\ &= \omega_{xx} s_k^2 + 2\omega_{xx} x s_k + \omega_{xz} s_k h(x) + \omega_x s_k. \quad (24)\end{aligned}$$

Since $h(x)$ is still involved in this phase shift calculation, to cope with this, we use a linear approximation to the phase distribution, where

$$\hat{\phi}(x, h(x)) = \omega_x x + \omega_z h(x) + \omega_0 \quad (25)$$

and the phase shift becomes

$$\hat{\theta}(x, h(x), s_k) = \hat{\phi}(x + s_k, h(x)) - \hat{\phi}(x, h(x)) = \omega_x s_k. \quad (26)$$

This approximation is valid for the surface profilometry in an orthographic projection system. For our high-resolution surface profilometry application under a perspective projection system in this paper, since the measuring range is small and the second-order coefficients are much smaller compared with the others in the P-PMP model, we can temporarily ignore the phases caused by $\omega_{xx} x^2$, $\omega_{xz} x h(x)$, and $\omega_{zz} h^2(x)$ and use this approximated orthographic model for initial height estimation.

As with the above, we can put this succinctly in a matrix form. Let

$$\hat{\mathbf{M}} = \begin{bmatrix} 1 & \cos\hat{\theta}(x, h(x), s_1) & -\sin\hat{\theta}(x, h(x), s_1) \\ 1 & \cos\hat{\theta}(x, h(x), s_2) & -\sin\hat{\theta}(x, h(x), s_2) \\ \vdots & \vdots & \vdots \\ 1 & \cos\hat{\theta}(x, h(x), s_n) & -\sin\hat{\theta}(x, h(x), s_n) \end{bmatrix} \quad (27)$$

$$\mathbf{v} = \begin{bmatrix} v_1 \\ v_2 \\ v_3 \end{bmatrix} = \begin{bmatrix} B(x) \\ C(x)\cos\phi(x, h(x)) \\ C(x)\sin\phi(x, h(x)) \end{bmatrix} \text{ and } \mathbf{i} = \begin{bmatrix} I_1(x) \\ I_2(x) \\ \vdots \\ I_n(x) \end{bmatrix}. \quad (28)$$

The condition number of the system matrix $\hat{M}$ is dependent on the displacements s_k. Choosing appropriate s_k's, such as by exhaustive search, can ensure that the system is well conditioned [15]. We then seek to minimize

$$\hat{E}(x, h(x)) = \|\hat{\mathbf{M}}\mathbf{v} - \mathbf{i}\|_2^2 \quad (29)$$

which leads to the analytical solution

$$\mathbf{v} = (\hat{\mathbf{M}}^T \hat{\mathbf{M}})^{-1} \hat{\mathbf{M}}^T \mathbf{i}. \quad (30)$$

From the second and third elements in $\mathbf{v}$ and the phase model in (25), we have

$$\hat{\phi}(x, h(x)) = \arctan\left\{\frac{v_3}{v_2}\right\}. \quad (31)$$

An initial estimate of the height is then

$$\hat{h}(x) = \frac{\hat{\phi}(x, h(x)) - (\omega_x x + \omega_0)}{\omega_z}. \quad (32)$$

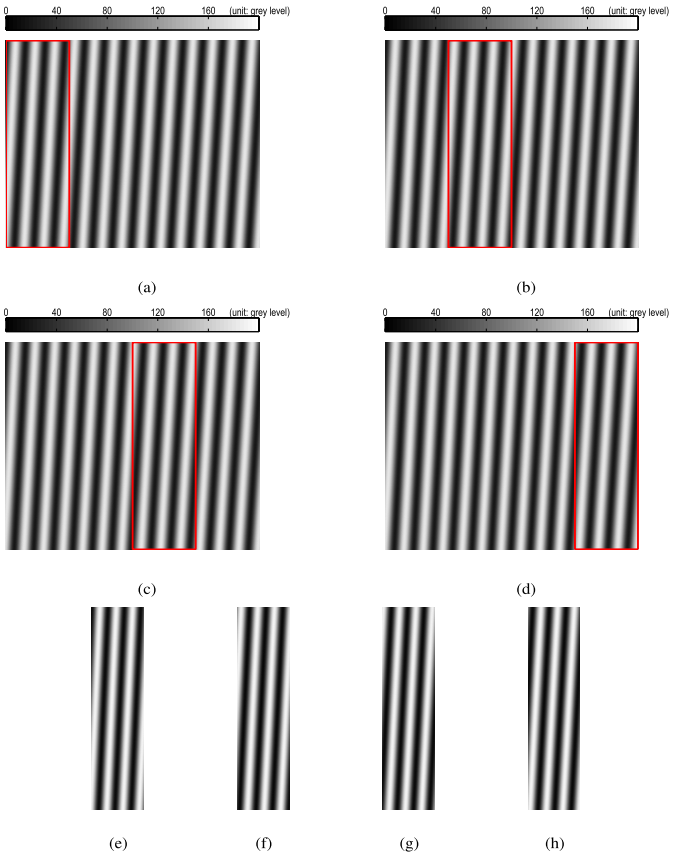

Fig. 5. (a)–(d) Image sequences of the tilted plane moving along the x-direction, and these marked regions correspond to the same physical location of the plane among the image sequences. (e)–(h) Aligned regions of interest extracted from the image sequences, and they are used for reconstructing the moving surface.

So far, up until the end of Step 2, this initial estimate of the height is based on the approximated phase shift computed with (26). Since the phase shift error would normally be interpreted as a phase offset due to the height variation in PMP, this approximated phase shift value would appear as a periodic error pattern in the reconstructed profile [29]. To reduce this error, we update the phase shift $\theta(x, h(x), s_k)$ by putting the initial height estimate $\hat{h}(x)$ into (24). Replacing $\hat{\theta}(x, h(x), s_k)$ with this updated phase shift, we reformulate the matrix $\hat{M}$, in a way similar to (27), and go through the steps from (29)–(31). Therefore, we have a refined phase value $\phi(x, h(x))$ for each reconstructed point.

Finally, in Step 4, we can solve for the height from the roots of the polynomial in (18) with the phase value obtained in the previous step, i.e., (33), as shown at the bottom of the page.

Since the coefficients of the second-order terms should be small, one of the two solutions above would not make practical sense, and by comparing them with the initial $\hat{h}(x)$. We then choose the correct one as the optimal solution

$$h(x) = \frac{-(\omega_{xz} x + \omega_z) \pm \sqrt{(\omega_{xz} x + \omega_z)^2 - 4\omega_{zz}[\omega_{xx} x^2 + \omega_x x + \omega_0 - \phi(x, h(x))]}}{2\omega_{zz}}. \quad (33)$$

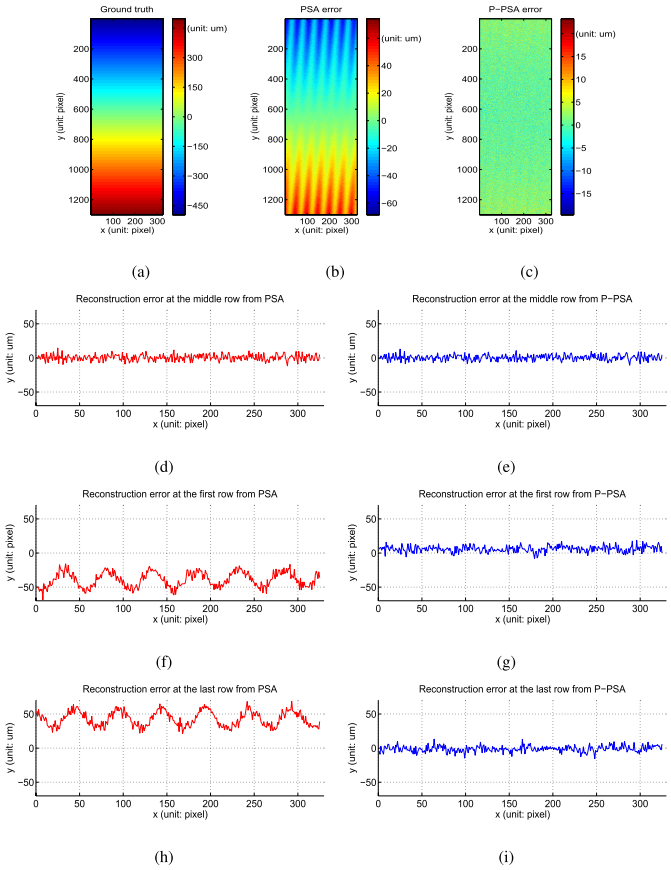

Fig. 6. Reconstruction results of a tilted plane. (a) Synthesized plane for reconstruction. (b) Reconstruction error with PSA. (c) Reconstruction error with P-PSA. (d)–(i) Sampled cross-sectional profiles of the reconstruction error with PSA and P-PSA.

for the reconstructed height. Furthermore, in a degenerated case with $\omega_{zz} = 0$, a unique solution is given by

$$h(x) = \frac{\phi(x, h(x)) - (\omega_{xx}x^2 + \omega_x x + \omega_0)}{\omega_{xz}x + \omega_z}. \tag{34}$$

The height of the whole surface can be reconstructed point-by-point in an analogous manner.

V. Experiments

A. Simulation Experiments

To compare the effectiveness of the proposed P-PSA with the conventional PSA for handling the perspective geometry effect during surface profilometry, we first simulate a perspective projection system similar to the one shown in Fig. 2, with $D = 1$ mm and $H = 10$ cm, a typical working condition for most of the semiconductor inspection and metrology applications. Let the light source pass through a sinusoidal grating whose period is 10 μm, with an incident angle $\alpha = 30°$ along the optical axis to the center of the reconstruction FOV, and then illuminate the reconstruction region whose magnification variation around 1% around the focal plane. Now, for each point (x_0), with the height $h(x_0)$ in the measuring space, we can calculate its ground-truth phase from (10) and the phase shift from (12) when the reconstructed object moves along the x-direction. To demonstrate the extent of the error caused by the perspective geometry effect, we simplify the other parameters, assuming the background intensity and the fringe contrast to be constants, where $B(x) = 100$ and $C(x) = 80$. Let the image size be 1300×1300 pixels, with a resolution of 10 μm per pixel. We then compute the image intensity for each reconstructed point by substituting the corresponding ground-truth phase into the imaging model in (21). For a fair comparison between P-PSA and PSA, we use $n = 4$ images for both methods, where the relative phase shifts $\theta(x, h(x), s_k)$ at the focal plane caused by the motion are $\{0, \pi/2, \pi, 3\pi/2\}$. Instead of calibrating the P-PMP model, using the above system parameters, we can derive our P-PMP model analytically according to (14). Considering the data normalization for the coefficients in this model, we translate the origin of the coordinate system be to at the center of the illuminated area at the focal plane. According to (16), we have the following P-PMP model:

$$\phi(x, h(x)) = 6.28 \times 10^{-6} x h(x) + 6.28 \times 10^{-2} x + 3.63 \times 10^{-2} h(x) + 362.76. \tag{35}$$

With this P-PMP model, we can then use the P-PSA in Section IV to reconstruct the surfaces of moving objects in this INSPECT system. In our first experiment, we limit the magnification variation to be no more than 1%. From (19) and (20), we can compute the measuring range of the height, which is limited between -497.51 and 497.51 μm. Therefore, we simulate a tilted homogeneous plane with these two extreme heights at the two boundaries. The captured images are shown in Fig. 5, where (a)–(d) correspond to the images of this moving homogeneous plane, and (e)–(h) show the subimages for the reconstructed surface after registration. Then, with an additive Gaussian noise having a standard deviation of $\sigma = 2$ intensity levels, we compare the surface profilometry using P-PSA versus the conventional PSA. The results are shown in Fig. 6.

By way of comparison, the ground truth of the tilted plane is shown in Fig. 6(a). By comparing the two reconstruction results with this, we can see that the proposed P-PSA has a better performance than PSA, shown in Fig. 6(b) and (c). In addition, three representative cross-sectional rows of the reconstruction error are plotted for comparison from Fig. 6(d)–(i). For the reconstructed points around zero height, both methods have good performance, as shown in Fig. 6(d) and (e). However, when the heights of the reconstructed points deviate much from the reference plane, such as at the boundaries of the tilted plane, the corresponding phase shift error in PSA increases due to magnification changes. This introduces a significant reconstructed error and results in a large periodical error pattern in the reconstruction results, as shown in Fig. 6(f) and (h). In contrast, the P-PMP model gives a better description of the phase distribution under a perspective system so that we can compensate the phase shift error for each reconstructed point and then obtain better results in Fig. 6(g) and (i). Numerically, the standard deviation of the reconstruction error are 24.8 and 5.0 μm for the PSA and the P-PSA, respectively.

TABLE I
STANDARD DEVIATIONS OF THE RECONSTRUCTION ERROR UNDER DIFFERENT NOISE LEVELS (UNIT: μm)

Magnification variation		noise level $\sigma = 1$	$\sigma = 2$	$\sigma = 3$	$\sigma = 5$	$\sigma = 7$	$\sigma = 10$
0.2%	PSA	5.4	6.8	8.6	12.8	17.3	24.3
	P-PSA	2.2	4.4	6.6	10.9	15.3	21.9
0.4%	PSA	10.0	10.8	12.1	15.4	19.3	25.7
	P-PSA	2.3	4.4	6.6	10.9	15.3	21.9
0.8%	PSA	19.6	20.0	20.7	22.8	25.6	30.8
	P-PSA	2.8	4.7	6.8	11.1	15.4	22.0
1.0%	PSA	24.4	24.8	25.4	27.1	29.5	34.1
	P-PSA	3.2	5.0	7.0	11.2	15.5	22.0
1.2%	PSA	29.2	29.5	30.0	31.5	33.5	37.7
	P-PSA	3.6	5.2	7.2	11.3	15.6	22.1

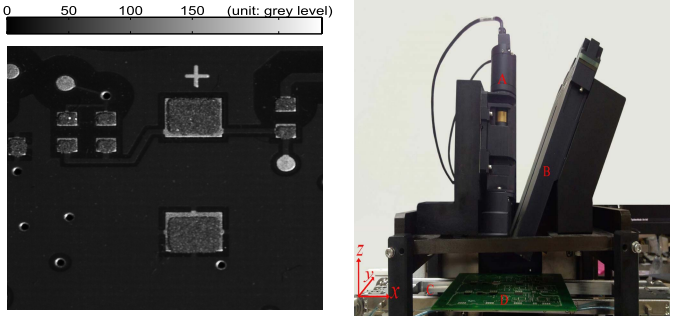

(a) (b)

Fig. 7. (a) 2-D image of a part of the PCB under inspection. (b) Physical setup of our INSPECT system. A: the imaging system, B: the projection system, C: the conveyor belt for transferring objects, and D: the PCB under inspection.

We carry out similar experiments with different noise levels and magnification variations. The details are shown in Table I. Consider first the case of a 1% magnification variation, which becomes a dominant error source in the PSA when reconstructing a moving surface. The standard deviation of the error increases mildly, from 24.4 to 34.1 μm, as the noise level increases. This is compared with the P-PSA method, where the phase shift error caused by the perspective geometry effect has been corrected, and therefore the random noise becomes the dominant error source, as evident from a significant increase from 3.2 to 22.0 μm at different noise levels. Likewise, we can observe similar trends with other magnification variations. The improvement from the P-PSA is significant over the PSA whenever the perspective geometry effect is a dominant error source. Furthermore, from each column of the table, the P-PSA error is quite close at different magnification variations. These comparison results verify the effectiveness of the proposed P-PSA for handling the perspective geometry effect when reconstructing moving surfaces.

B. Experiments in Real Applications

In the semiconductor assembly industry, SMT has become a much faster automatic assembly process than traditional

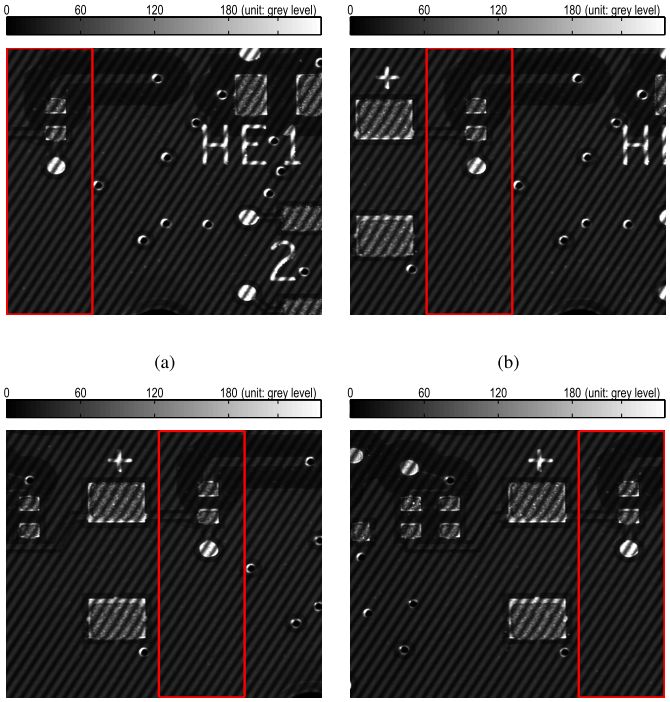

Fig. 8. (a)–(d) Four sequential fringe pattern images of the PCB when it is moving across the INSPECT system. With these images, the surface of the solder paste and the PCB within their common physical region, marked in red, can be reconstructed.

through-hole technology. With this technology, the surface-mount devices (SMD), whose sizes are as small as several hundred micrometers, can be soldered to the printed circuit board (PCB) precisely. However, the connectivity between the SMD and the PCB is greatly affected by the quality of the solder paste, and the majority of the defects, such as solder bridges and insufficient deposits of solder paste, are caused by the printing process. Therefore, solder paste inspection has become a necessary step on the automatic assembly line for PCBs.

Nowadays, most of the solder paste inspection systems only use the intensity image for defect detection. Fig. 7(a) shows an intensity image of a part of a PCB. From this 2-D image, we can extract the positions of holes, pads on the PCB and detect the solder paste on some of the pads. However, some detailed 3-D information such as the flatness of the PCB, the height and the volume of the solder paste cannot be obtained for a full inspection. Furthermore, most of these systems assume the PCB to be stationary during inspection [30], and require a complex motion system to move the bulky vision system to different regions of a large PCB to inspect the solder paste region-by-region. This kind of inspection process complicates the design of the motion system and increases the cycle time. Hence, they are not suitable for some high-speed applications on the production line. Therefore, we develop an INSPECT system for solder paste inspection. Fig. 7(b) shows the physical setup of our INSPECT system, where we use the cameras and projectors made by ASM Pacific Technology

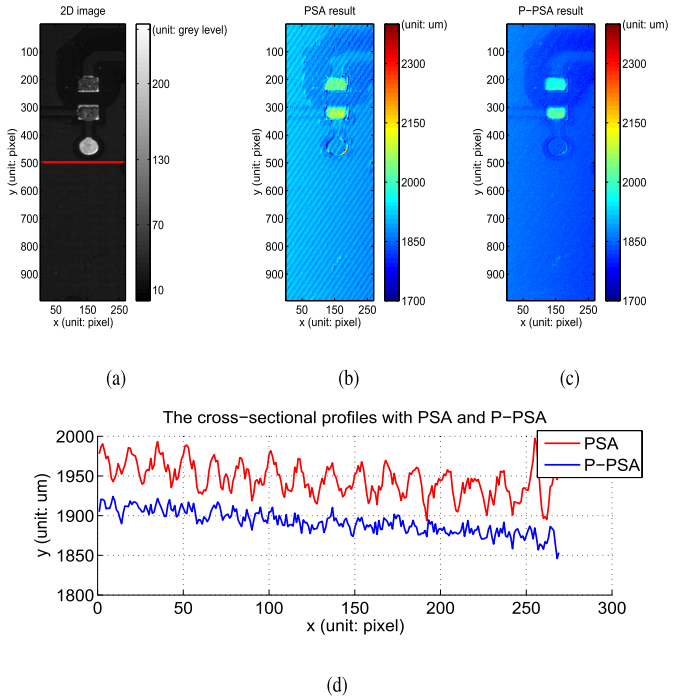

Fig. 9. (a) Image of the reconstructed region without fringe patterns. (b) and (c) Surface reconstruction results with PSA and P-PSA, respectively. (d) Cross-sectional profiles of the middle row in this reconstructed region, marked in red in (a).

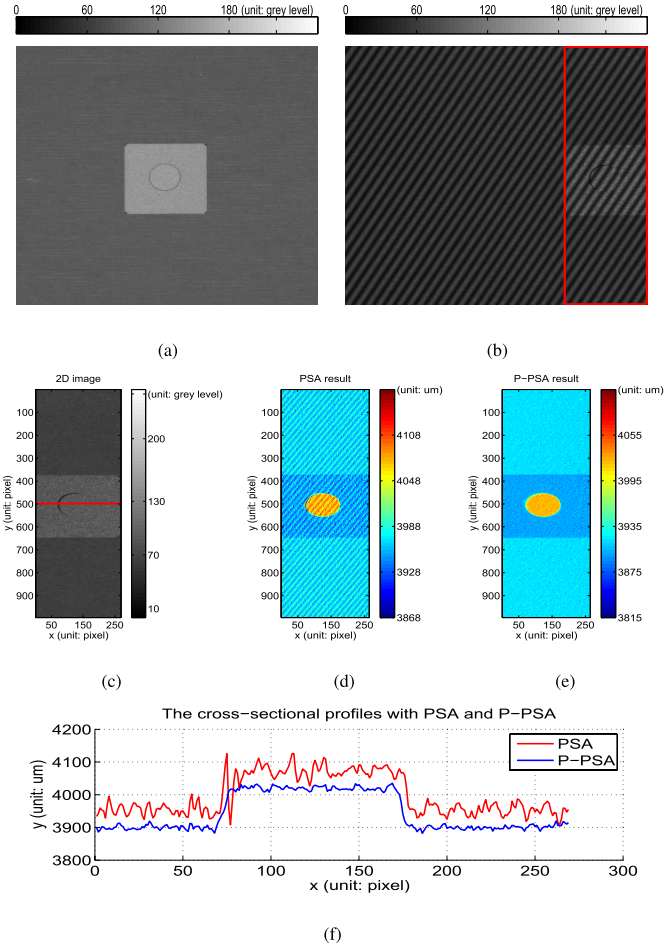

Fig. 10. (a) Image of the golden sample for accuracy verification. (b) One of the fringe images for surface profilometry. (c) Reconstructed region for comparison. (d) and (e) Surface reconstruction results with PSA and P-PSA, respectively. (f) Cross-sectional profiles along the centering row marked in red in (c).

Limited. Each camera with a sensor array 1000×1000, covers a 15 mm $\times$ 15 mm FOV. Correspondingly, each projector on the right side projects a fixed sinusoidal pattern onto the same FOV. Thus, there is no synchronization problem between the camera and the corresponding projector. Assuming that the conveyor belt moves along the x-direction, when the PCB is translated by the conveyor belt to the FOV of the INSPECT system, the image sequences of the PCB are captured for inspection and the measuring range is extended automatically along this direction. On its orthogonal direction, i.e., along the y-axis, camera arrays and projector arrays can be arranged in lines to extend the measuring range, as illustrated in our setup with dual cameras and projectors.

For calibrating the camera system, we put a calibration glass with 1000-μm checkerboard patterns at different spatial configurations and adopt Zhang's method for estimating the intrinsic and extrinsic parameters [31]. The calibrated resolution is 14.9 μm per pixel in our system. The intrinsic and extrinsic parameters for the projector can be further estimated by an extra programmable LCD panel [24], but we do not use these parameters directly in the proposed method since only the phase values on the whole measuring space are needed for surface profilometry. Hence, we just put a stationary homogenous plane at different heights to calibrate the phase distribution on the measuring space as shown in Section IV. After calibration, the fringe period of the projected sinusoidal pattern on the reference plane of this system is 500 μm along the x-direction. For surface profilometry of the moving PCB, we capture the images of the PCB at every 3625 μm along the conveyor belt so that the resulting phase shifts are $\{0, \pi/2, \pi, 3\pi/2\}$ on the focal plane after the modulus operator on 2π. Fig. 8 shows a set of such fringe pattern images when the PCB moves across the FOV. Then, we use the conventional PSA and the P-PSA to reconstruct the surface of the overlapped region among these images. Fig. 9(a) shows the reconstruction results. We find that the surface of the PCB under inspection is not exact on the focal plane of the vision system due to the thicknesses of the PCB. In real system, the imperfect installation of the conveyor belt may also cause an offset of the reconstructed surface from the focal plane. These deviations result in the magnification variations and the phase shift error under a perspective projection system. Hence, there is a periodical error pattern on the reconstructed surface from PSA, as shown in Fig. 9(b). However, in the proposed P-PSA, we can compensate the phase shift error caused by the perspective geometry effect during surface profilometry and then obtain a better reconstruction result in Fig. 9(c). We also compare the reconstructed cross-sectional profiles across a flat region of PCB in Fig. 9(d), where most of the error ripple is removed by our P-PSA. To verify the acquired height with the ground truth, a golden sample of a steel cylinder has been fabricated and shown in the centering region of Fig. 10(a). Its diameter is 1500 μm and its height relative to the nearby homogenous substrate plane is 120 μm.

Fig. 10(b) is one of the fringe images when this golden sample is moving across the FOV for surface profilometry. Similarly, we use both methods to reconstruct the surface of within the region in Fig. 10(c) and compare their cross-sectional profiles in the center, as shown in Fig. 10(d)–(f). We see that similar ripples exist in the PSA method. To measure the accuracy of each method, we fit a plane based on reconstructed profile of the substrate and then calculate the heights of cylinder as the projected distances from the top surface of cylinder to this fitted plane. The means of heights are 120.7 and 117.8 μm from the P-PSA and the PSA method. The corresponding standard deviations of the error are 6.6 and 28.4 μm, respectively.

Based on this improved surface profile from the proposed method, we can accomplish further 3-D metrology and inspection tasks for the PCB and feed this information back timely for improving the printing process and the first-past test yield. In our INSPECT system, we use Intel Core i7 CPU X 980 @ 3.33 GHz with 4-G RAM in the computational system, and we can finish dense surface reconstruction within 50 ms per 15 mm $\times$ 15 mm FOV. While the conventional solder paste inspection system takes several hundred milliseconds to move the optical system, and then stops at the expected position before inspection. Therefore, the proposed INSPECT system is suitable for most of the real-time dense surface inspection applications in the semiconductor industry.

VI. Conclusion

In this paper, we report an INSPECT system, which only projects a single sinusoidal pattern on a moving object for surface profilometry. This reduces the complexity of optics design for the projection system, and the whole INSPECT system is suitable for surface metrology and inspection of moving objects on the production line.

References

[1] Y. Li, Y. F. Li, Q. L. Wang, D. Xu, and M. Tan, "Measurement and defect detection of the weld bead based on online vision inspection," *IEEE Trans. Instrum. Meas.*, vol. 59, no. 7, pp. 1841–1849, Jul. 2010.

[2] P. Lam and E. Lam, *Soaring Like Eagles: ASM's High-Tech Journey in Asia*. New York, NY, USA: Wiley, 2006.

[3] J. D. Plummer, M. Deal, and P. D. Griffin, *Silicon VLSI Technology: Fundamentals, Practice, and Modeling*. Englewood Cliffs, NJ, USA: Prentice-Hall, 2000.

[4] E. Y. Lam and A. K. Wong, "Computation lithography: Virtual reality and virtual virtuality," *Opt. Exp.*, vol. 17, no. 15, pp. 12259–12268, Jul. 2009.

[5] F. Blais, "Review of 20 years of range sensor development," *J. Electron. Imag.*, vol. 13, no. 1, pp. 231–240, Jan. 2004.

[6] G. Zeng, Y. Matsushita, L. Quan, and H.-Y. Shum, "Interactive shape from shading," in *Proc. IEEE Comput. Soc. Conf. Comput. Vis. Pattern Recognit.*, Jun. 2005, pp. 343–350.

[7] D. Scharstein and R. Szeliski, "A taxonomy and evaluation of dense two-frame stereo correspondence algorithms," *Int. J. Comput. Vis.*, vol. 47, no. 1, pp. 7–42, May 2002.

[8] S. K. Nayar and Y. Nakagawa, "Shape from focus: An effective approach for rough surfaces," in *Proc. IEEE Int. Conf. Robot. Autom.*, vol. 1. May 1990, pp. 218–225.

[9] Y. Zhuang, N. Jiang, H. Hu, and F. Yan, "3-D-laser-based scene measurement and place recognition for mobile robots in dynamic indoor environments," *IEEE Trans. Instrum. Meas.*, vol. 62, no. 2, pp. 438–450, Feb. 2013.

[10] S. Hussmann and T. Liepert, "Three-dimensional TOF robot vision system," *IEEE Trans. Instrum. Meas.*, vol. 58, no. 1, pp. 141–146, Jan. 2009.

[11] F. Deng, J. Liu, J. Deng, K. S. Fung, and E. Y. Lam, "A three-dimensional imaging system for surface profilometry of moving objects," in *Proc. IEEE Int. Conf. Imag. Syst. Techn.*, Oct. 2013.

[12] R. Leach, *Optical Measurement of Surface Topography*, 1st ed. Berlin, Germany: Springer-Verlag, 2011.

[13] F. Deng *et al.*, "Illumination-invariant phase-shifting algorithm for three-dimensional profilometry of a moving object," *Opt. Eng.*, vol. 51, no. 9, p. 097001, Sep. 2012.

[14] Y. Hu, J. Xi, Z. Yang, E. Li, and J. Chicharo, "Study on generalized analysis model for fringe pattern profilometry," *IEEE Trans. Instrum. Meas.*, vol. 57, no. 1, pp. 160–167, Jan. 2008.

[15] F. Deng, W. F. Sze, J. Deng, K. S. Fung, W. Leung, and E. Y. Lam, "Regularized multiframe phase-shifting algorithm for three-dimensional profilometry," *Appl. Opt.*, vol. 51, no. 1, pp. 33–42, Jan. 2012.

[16] L. Biancardi, G. Sansoni, and F. Docchio, "Adaptive whole-field optical profilometry: A study of the systematic errors," *IEEE Trans. Instrum. Meas.*, vol. 44, no. 1, pp. 36–41, May 2009.

[17] C. P. Brophy, "Effect of intensity error correlation on the computed phase of phase-shifting interferometry," *J. Opt. Soc. Amer. A*, vol. 7, no. 4, pp. 537–541, Apr. 1990.

[18] K. Liu, Y. Wang, D. L. Lau, Q. Hao, and L. G. Hassebrook, "Gamma model and its analysis for phase measuring profilometry," *J. Opt. Soc. Amer. A*, vol. 27, no. 3, pp. 553–562, Mar. 2010.

[19] Y. Hu, J. Xi, J. Chicharo, W. Cheng, and Z. Yang, "Inverse function analysis method for fringe pattern profilometry," *IEEE Trans. Instrum. Meas.*, vol. 58, no. 9, pp. 3305–3314, Sep. 2009.

[20] M. Gupta and S. K. Nayar, "Micro phase shifting," in *Proc. IEEE Conf. Comput. Vis. Pattern Recognit. (CVPR)*, Jun. 2012, pp. 1–8.

[21] Z. Wang and B. Han, "Advanced iterative algorithm for phase extraction of randomly phase-shifted interferograms," *Opt. Lett.*, vol. 29, no. 14, pp. 1671–1673, Jul. 2004.

[22] S. Gai and F. Da, "Fringe image analysis based on the amplitude modulation method," *Opt. Exp.*, vol. 18, no. 10, pp. 10704–10719, May 2010.

[23] J. Degrieck, W. V. Paepegem, and P. Boone, "Application of digital phase-shift shadow moire to micro deformation measurements of curved surfaces," *Opt. Lasers Eng.*, vol. 36, no. 1, pp. 29–40, Jul. 2001.

[24] Z. Song and R. Chung, "Use of LCD panel for calibrating structured light-based range sensing system," *IEEE Trans. Instrum. Meas.*, vol. 57, no. 11, pp. 2623–2630, Nov. 2008.

[25] C. D'Argenio, G. D. Leo, C. Liguori, and A. Paolillo, "A simplified procedure for the calibration of a fringe pattern profilometer," in *Proc. IEEE Int. Instrum. Meas. Technol. Conf.*, Oct. 2009, pp. 652–657.

[26] S. R. Buss, *3D Computer Graphics: A Mathematical Introduction With OpenGL*. Cambridge, U.K.: Cambridge Univ. Press, May 2003.

[27] R. Anchini, G. D. Leo, C. Liguori, and A. Paolillo, "A new calibration procedure for 3-D shape measurement system based on phase-shifting projected fringe profilometry," *IEEE Trans. Instrum. Meas.*, vol. 58, no. 5, pp. 1291–1298, May 2009.

[28] M. Takeda, H. Ina, and S. Kobayashi, "Fourier-transform method of fringe-pattern analysis for computer-based topography and interferometry," *J. Opt. Soc. Amer. A*, vol. 72, no. 1, pp. 156–160, Jan. 1982.

[29] F. Deng, C. Liu, W. Sze, J. Deng, K. S. Fung, and E. Y. Lam, "A polynomial phase-shift algorithm for high precision three-dimensional profilometry," *Proc. SPIE*, vol. 8661, p. 866102, Feb. 2013.

[30] J. Jiang, J. Cheng, and D. Tao, "Color biological features-based solder paste defects detection and classification on printed circuit boards," *IEEE Trans. Compon. Packag. Manuf. Technol.*, vol. 2, no. 9, pp. 1536–1544, Sep. 2012.

[31] Z. Zhang, "A flexible new technique for camera calibration," *IEEE Trans. Pattern Anal. Mach. Intell.*, vol. 22, no. 11, pp. 1330–1334, Nov. 2000.

Fuqin Deng received the B.S. degree in applied mathematics from the Harbin Institute of Technology, Harbin, China, in 2005, the M.S. degree in control science and engineering from the Shenzhen Graduate School of Harbin Institute of Technology, Shenzhen, China, in 2007. He is currently pursuing the Ph.D. degree with the Department of Electrical and Electronic Engineering, University of Hong Kong, Hong Kong.

His current research interests include image processing, pattern recognition, computer vision, and machine vision applications.

Chang Liu received the B.S. degree in information systems from Nankai University, Tianjin, China, in 2003, the M.S. degree in applied mathematics from Sun Yat-sen University, Guangzhou, China, in 2006, and the Ph.D. degree from the Department of Computer Science, Hong Kong Baptist University, Hong Kong.

His current research interests include pattern recognition, computer vision, and machine learning.

Wuifung Sze received the B.Eng. (Hons.) degree in electronic and communications engineering, and the M.Phil. and M.Stat. (Hons.) degrees from the University of Hong Kong, Hong Kong.

He was a System Engineer with Octopus Card Ltd., Hong Kong, before he joined the ASM Pacific Technology Ltd., Hong Kong, where he is currently a Technical Manager responsible for developing vision systems for high-precision metrology applications.

Jiangwen Deng is a Senior Technical Manager with the Department of Research and Development, ASM Pacific Technology Ltd., Hong Kong. His current research interests include pattern recognition and computer vision.

Kenneth S. M. Fung received the Ph.D. degree from the Department of Electrical and Electronic Engineering, University of Hong Kong, Hong Kong, in 1999.

He joined ASM Pacific Technology Ltd., Hong Kong, as a Senior Engineer, where he is a Senior Technical Manager with the Department of Research and Development. He developed a subpixel-accuracy, high-speed, and robust computer vision alignment algorithm that was applied in all ASM products and boosted the capability and vision technology level of the company's semiconductor packaging machines. He currently leads a team of research engineers responsible for the projects in machine vision inspection and algorithm development. He also provides technical supervision for a team of vision application engineers who are responsible for the projects in developing machine vision applications on ASM products. His current research interests include computer vision, pattern recognition, digital image processing, and artificial neural networks.

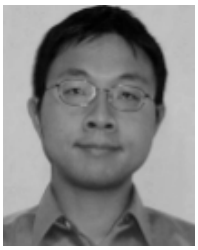

Edmund Y. Lam (M'00–SM'05) received the B.S. (with distinction), M.S., and Ph.D. degrees in electrical engineering from Stanford University, Stanford, CA, USA.

He is currently a Professor of Electrical and Electronic Engineering and the Director of the Computer Engineering Program with the University of Hong Kong, Hong Kong, where he is also the Founding Director of the Imaging Systems Laboratory. His current research interests include the theme of computational optics and imaging, in particular, its applications in semiconductor manufacturing and biomedical systems.

Dr. Lam is a Fellow of the Optical Society of America and the International Society for Optics and Photonics. He is currently a Topical Editor of the *Journal of the Optical Society of America A*, and an Associate Editor of the IEEE TRANSACTIONS ON BIOMEDICAL CIRCUITS AND SYSTEMS and the IEEE SIGNAL PROCESSING LETTERS.